Biomaterials Science

ROYAL SOCIETY OF CHEMISTRY

PAPER

View Article Online
View Journal | View Issue

Cite this: *Biomater. Sci.*, 2023, **11**, 3589

S–Cu–FC/CuS modified GO carboxymethyl cellulose hydrogel for enhanced photocatalytic sterilization through homo-heterojunction interface accelerated charge transfer†

Bo Huang,‡[a,f] Wei Guan,‡[b] Chaofeng Wang,[c] Shuilin Wu, *[b,d,f] Zhenduo Cui,[b] Yufeng Zheng, [d] Zhaoyang Li, [b] Shengli Zhu, [b] Hui Jiang, [b] Paul K. Chu [e] and Xiangmei Liu*[c]

Charge transfer and separation play a critical role in the photocatalytic efficiency of photoresponsive materials and their subsequent applications. Herein, for the first time, we constructed a homo-heterostructured S–Cu–FC/CuS modified carboxymethyl cellulose (CMC) hydrogel doped with graphene oxide (GO) (S–Cu–FC/CuS/GO@CMC) through an *in situ* ionic complexation reaction, which exhibited enhanced photocatalytic performance under 808 nm near-infrared (NIR) light irradiation. On the one hand, photo-excited charges can rapidly transfer across the homo-heterojunction interface with copper atoms in S–Cu–FC/CuS as both donors and acceptors. On the other hand, the interface between GO and S–Cu–FC/CuS also favors the fast transfer of photogenerated charges. Hence, with the assistance of a photothermal effect, the enhanced photocatalytic performance of S–Cu–FC/CuS/GO endowed the hydrogel with robust sterilization ability for killing 99.5% *S. aureus* and 100.0% *E. coli* under 10 min NIR light irradiation. An *in vivo* test disclosed that this hydrogel could also accelerate the healing of bacteria-infected wounds.

Received 16th February 2023,
Accepted 17th March 2023

DOI: 10.1039/d3bm00260h

rsc.li/biomaterials-science

1. Introduction

The serious threat posed by infectious diseases has had a constant impact on worldwide public health defences.[1–3] For example, the continuing epidemic of COVID-19 has caused severe damage to the development of the worldwide economy and deprived more than 6.5 million people in the world of their lives,[4,5] for which clinical reports indicated that the leading cause of death was bacterial infections and subsequent complications due to the weakened immune system attacked by the virus.[5,6] Unlike viruses, bacteria can invade bodies from a defective surface and the surrounding tissues will be used as a medium for proliferation. A skin wound means there is no physical barrier and it will be a superb entrance for bacterial invasion of tissues or blood vessels.[7] Although antibiotic treatment is the most common way to combat bacterial infections in clinical practice, it can take a long time and may lead to drug resistance, thus inducing inflammation and other side-effects.[8] That can be torturous for patients, especially those with diabetes or haemophilia.[9] Therefore, non-antibiotic therapy is a priority and there is an urgent need for it in the face of the huge costs and long cycle for developing new antibiotics.

Lately, phototherapies based on photo-responsive materials have been extensively investigated as an alternative to antibiotic treatment because of their rapid, highly effective and non-invasive characteristics.[10] By photothermal conversion and/or a photocatalytic effect, photo-responsive materials can produce heat and/or reactive oxygen species (ROS) in a short time under light irradiation to kill bacteria without drug resistance.[10] For instance, metal–organic frameworks,[11–13] MXenes,[14,15] Ag_2S quantum dots,[16] and other materials have

[a]*College of pharmacy, Guangxi University of Chinese Medicine, Nanning 530022, China*
[b]*School of Materials Science & Engineering, the Key Laboratory of Advanced Ceramics and Machining Technology by the Ministry of Education of China, Tianjin University, Tianjin, 300072, China*
[c]*School of Health Science and Biomedical Engineering, Hebei University of Technology, Tianjin, 300401, China. E-mail: Liuxiangmei1978@163.com*
[d]*School of Materials Science & Engineering, Peking University, Beijing, 100871, China. E-mail: slwu@pku.edu.cn*
[e]*Department of Physics, Department of Materials Science and Engineering, and Department of Biomedical Engineering, City University of Hong Kong, Kowloon, Hong Kong, 999077, China*
[f]*Biomedical Materials Engineering Research Centre, Hubei University, Wuhan 430062, China*

†Electronic supplementary information (ESI) available. See DOI: https://doi.org/10.1039/d3bm00260h

‡These authors contribute equally to this paper.

been reported to be employed for treating *in vivo* diseases by photothermal therapy (PTT), photodynamic therapy (PDT) or a synergy of both PTT and PDT.[7,17–24] However, PDT is often mainly affected by the photocatalytic performance of the materials. On the one hand, the rapid recombination between separated e^- and h^+ will take place continuously during the movement of e^- from the inside to surfaces or interfaces. On the other hand, the low transfer rate of photogenerated carriers will also lead to their consumption before they can participate effectively in photocatalytic reactions.[24–28] The two factors impair the photocatalytic performance, thus reducing the yields of ROS. To improve this situation, many strategies have been used, such as defect-rich design, series connections between heterojunctions or substance doping into interfaces, but these methods usually involve more complex processes.[24–28] Therefore, it is necessary to realize the faster and more efficient transfer of electrons in a heterojunction or interface with a simple strategy.

CuFC is a ferrocyanide, and these compounds are all formed by the complexing of different transition metal ions and $[Fe(CN)_6]^{4-}$.[29–32] For instance, Prussian blue (PB) is the most typical one, which has been approved by FDA for biomedicine.[33–36] Due to the formation of coordination bonds between organic molecules and metal ions, a large number of structures with periodically ordered arrangements or pore structures similar to a metal–organic framework will be formed. Therefore, ferrocyanides possess good selective adsorption ability for heavy metal ions and are often used to adsorb and remove heavy metal ions from water or human organs.[29–32] Moreover, because of chemical inertness, most ferrocyanides are different from PB and cannot be endowed with photothermic activity or photocatalysis through ion doping or loading with a photosensitizer.[33–36] Therefore, if this industrial adsorption material could be endowed with photocatalytic performance, there would be a series of novel photocatalytic agents and the potential range of application of ferrocyanides would be greatly expanded, such as photo-controlled water disinfection, and *in vivo* photo-controlled lesion elimination.

Herein, inspired by the metal elements of copper ferrocyanide (CuFC), we for the first time synthesized a homologous heterojunction of S–Cu–FC/CuS by an *in situ* ionic complexation reaction with the feasible addition of thioacetamide (TAA). This homo-heterostructured S–Cu–FC/CuS exhibited excellent photocatalytic activity under 808 nm NIR light irradiation due to the accelerated production of photogenerated carriers and faster transfer with copper atoms as both donors and acceptors simultaneously. The following encapsulation of S–Cu–FC/CuS by GO-doped carboxymethyl cellulose (CMC) hydrogel induced the formation of the hybrid hydrogel S–Cu–FC/CuS/GO@CMC (labelled HH hydrogel), which exhibited a better photocatalytic property than S–Cu–FC/CuS because GO could act as an acceptor of photogenerated carriers and consequently improve the separation rate of electron–hole pairs. The improved photocatalytic property and photothermal effect endowed the HH hydrogel with rapid and highly effective sterilization ability under 808 nm NIR light irradiation.

2. Experimental section

2.1. Reagents

Potassium ferrocyanide trihydrate ($K_4Fe(CN)_6{\cdot}3H_2O$), copper sulfate pentahydrate ($CuSO_4{\cdot}5H_2O$), sodium dodecylbenzene sulfonate (SDS) and thioacetamide (TAA) were purchased from Sigma-Aldrich Inc. (USA). Carboxymethyl cellulose (CMC), acrylic acid, ammonium persulfate and *N*,*N*-dimethyldiacrylamide (PDMA) were purchased from Shanghai Aladdin Biochemical Technology Co. (China). Graphene oxide (GO) was purchased from Shenzhen TuLing Evolution Technology Co. (China). Ethanol was purchased from LongXi Chemical Reagent Co. (China).

2.2. Preparation of CuFC

$K_4Fe(CN)_6{\cdot}3H_2O$ (84.4 mg) and $CuSO_4{\cdot}5H_2O$ (100 mg) were fully dissolved in 20 mL of deionized water, respectively. After blending the two solutions, SDS (50 mg) was added and the mixed solution was reacted at 80 °C for 6 h. The reacted turbid liquid was washed three times with deionized water; then lyophilized to obtain pure CuFC powder.

2.3. Preparation of S–Cu–FC/CuS

CuFC (20 mg) and TAA (10 mg) were added into a mixed liquid (20 mL, water : ethanol = 3 : 1). The pH of the mixture was adjusted to 5 and it was stirred at 60 °C for 30 min. After the reaction, the solution was washed with ethanol and deionized water three times and lyophilized to obtain S–Cu–FC/CuS powder.

2.4. Preparation of CMC hydrogel and GO@CMC hydrogel

CMC (2 g) was fully dissolved in aqueous GO (40 mL, 0.5 mg mL^{-1}) with magnetic stirring at 60 °C. Then, acrylic acid (2 mL), ammonium persulfate (80 mg) and PDMA (60 mg) were added successively and magnetic stirring was withdrawn. Then, the mixture was held at 80 °C for 4 h to achieve gelation. Finally, the GO@CMC hydrogel was dehydrated at 100 °C for a whole night. The CMC hydrogel could be obtained through the same method.

2.5. Preparation of S–Cu–FC/CuS/GO@CMC hybrid hydrogel (HH hydrogel)

The GO@CMC hydrogel was cut into uniform blocks (3 × 3 × 3 mm^3) and soaked in an S–Cu–FC/CuS dispersion solution (2 mL, 1 mg mL^{-1}) for 30 min. This HH hydrogel was rinsed twice with deionized water.

2.6. Preparation of S–Cu–FC/CuS/GO

CuFC (1.433 mg) and CuS (0.674 mg) were mixed and ground. The mixture was treated with ultrasound for 2 h and dispersed in ethanol and lyophilized to obtain CuFC/CuS. More details can be found in the ESI.†

2.7. Characterization

The microtopography of the NPs or hydrogels was observed with a high-resolution electron microscope (TEM, JEOL-2100F,

Japan) or field emission scanning electron microscope (FESEM, ZEISS Sigma 500, Germany). The particle sizes of the samples were detected by dynamic light scattering analysis (DLS, 90 Plus/BIMAS, Brookhaven, USA). X-ray diffractometry (XRD, D8 Advance, Germany) was used to determine the XRD patterns of CuFC and S–Cu–FC/CuS. Confocal Raman microspectroscopy (Renishaw, UK) was used to obtain the Raman spectra of CuFC and S–Cu–FC/CuS. The elements on the surfaces of the hydrogels were determined by X-ray photoelectron spectroscopy (XPS, Thermo Fisher Scientific 250Xi, USA). An ultraviolet–visible (UV–vis) spectrophotometer (UV-2700, Shimadzu, Japan) was used to record the UV spectra. The temperature changes of different samples under 808 nm near-infrared (NIR) light irradiation were recorded with a thermal imager (FILR E50, USA).

2.8. Tensile and compression analyses of the hydrogels

The tensile and compression analyses of the different hydrogels were determined with a universal tensile machine (CMT4104, USA). First, the hydrogels were shaped into blocks (width = 25 mm, length = 25 mm, thickness = 5 mm) for the tensile test (loading rate = 50 mm min^{-1}, gauge length between clamps = 20 mm). Secondly, the hydrogels were shaped into columns (height = 15 mm, basal diameter = 6 mm) for the pressure test (maximum compression distance = 5 mm). The fixture did not return to its original position at the end of the test.

2.9. Swelling ratio test of the hydrogels

After being dried, the hydrogels were cut into blocks (weight = 500 ± 50 mg) and labelled (g_0) and then soaked in deionized water. After soaking, the hydrogels were removed from the solvents and weighed at specific times (10, 20, 30, 40 and 50 h), and they were labelled g_t. All the swelling ratios were calculated according to the following equation: Swelling ratio (%) = $(g_t - g_0)/g_0 \times 100\%$.

2.10. Release detection of Cu^{2+} and Fe^{2+} *in vitro*

To obtain the release trend of Cu^{2+} and Fe^{2+} from the S–Cu–FC/CuS/GO@CMC hybrid hydrogel, the HH hydrogel was immersed in PBS (20 mL). After soaking for a specific time (0, 1, 2, 3, 4, 5, 6, 7, 8, 9, 10, 11, 12, 13, and 14 days), a fixed volume of liquid was removed from PBS to test the c(Cu^{2+}) and c(Fe^{2+}) and fresh PBS was added to ensure a 2 mL volume of liquid. The amount of released Cu^{2+} and Fe^{2+} was determined with an inductively coupled plasma optical emission spectrometer (ICP-OES, PQ9000, Analytik Jena, Germany).

2.11. Photothermal effect test

The photothermal effects of the hydrogels and NPs were evaluated by recording the temperature changes of the samples under 808 nm NIR light irradiation (0.6 W cm^{-2}) for 10 min. The stability of the photothermal effect was studied by recording the temperature changes of the HH hydrogel under NIR light irradiation for four off–on cycles (10 min heating and 10 min cooling).

2.12. Photodynamic effect test

DCFH-DA probe test. ROS-sensitive dichlorofluorescein diacetate (DCFH-DA) was used to detect ROS generation by samples under 808 nm NIR light irradiation (0.6 W cm^{-2}). The GO@CMC hydrogel (3 × 3 × 3 mm^3) was immersed in an S–Cu–FC/CuS (2 mL, 1 mg mL^{-1}) dispersion for 30 min and the obtained HH hydrogel was rinsed twice with deionized water. After the immersion process, the liquid was then collected for lyophilization and the residual powder weighed. The above steps were repeated three times and the loading rate of the heterojunction nanoparticles in the hydrogel was calculated as 50%. Then, the HH hydrogel (3 × 3 × 3 mm^3), GO@CMC hydrogel (3 × 3 × 3 mm^3), S–Cu–FC/CuS NPs (1 mg, 1 mg mL^{-1}), and CuFC NPs (1 mg, 1 mg mL^{-1}) were exposed to 808 nm NIR light irradiation for 10 min. The fluorescence intensity of the solutions was recorded by a multifunctional microporous plate detector (SprectraMax®i3, Molecular Devices, USA) with excitation at 488 nm and emission at 670 nm.

Electron spin resonance spectroscopy (ESR). The hydrogel samples were cut into blocks (3 × 3 × 3 mm^3) and prepared for testing after the same immersion process as in the fluorescent probe test above. Then, samples of HH hydrogel (3 × 3 × 3 mm^3), CuS (1 mL, 1 mg mL^{-1}), and S–Cu–FC/CuS (1 mL, 1 mg mL^{-1}) were mixed with spin-trapping agent solutions (2,2,6,6-tetramethylpiperidine (TEMP)), respectively. 200-μL of TEMP (50 mM, 180 μL H_2O) was used to detect $^1O_2$ generation by the samples under irradiation by 808 nm NIR light (0.6 W cm^{-2}) for 10 min by a spectrometer (JES-FA200, JEOL, Japan) to record the ESR spectra. The curve of pure TEMP irradiated by 10 min NIR light was set up as the control group.

2.13. Density-functional-theory (DFT) calculations

The Vienna *Ab initio* Package (VASP) was employed to process DFT calculations within the generalized gradient approximation (GGA) using the PBE formulation. The projected augmented wave (PAW) potentials were chosen to describe the ionic cores and take valence electrons into account using a plane wave basis set with a kinetic energy cutoff of 400 eV. The partial occupancies of Kohn–Sham orbitals were allowed to employ the Gaussian smearing method (width = 0.05 eV). The electronic energy was considered self-consistent when the energy change was smaller than 10–5 eV. A geometric optimization was considered convergent when the force change was smaller than 0.02 eV $Å^{-1}$. Grimme's DFT-D3 methodology was used to describe the dispersion interactions. Then, by using a Monkhorst–Pack *k*-point (9 × 9 × 5) grid for Brillouin zone sampling, the equilibrium lattice constants of the hexagonal CuS unit cell were optimized to be $a = b = 2.895$ Å and $c = 6.180$ Å. Similarly, by using a Monkhorst–Pack *k*-point (2 × 2 × 2) grid for Brillouin zone sampling, the equilibrium lattice constant of the cubic CuFC unit cell was optimized to be $a = b = 9.991$ Å. Next, these unit cells were used to construct a surface model of the heterojunction and an interface between CuFC (110) and CuS (001). There was a periodicity ($p(7 \times 7)$) in

the part of CuFC (110) in the x and y directions, and another 2 stoichiometric layers in the z direction. There were 16 Fe, 32 Cu, 96 C and 96 N atoms. There was a periodicity ($p(3 \times 5\sqrt{3})$) in the part of CuS (001) in the x and y directions, and another 1 stoichiometric layer in the z direction. There were 60 Cu and 60 S atoms. The CuFC (110)/CuS (001) heterojunction was separated by a vacuum layer in the z direction with a depth of 15 Å to separate the surface slab from its periodic duplicates. The gamma point in the Brillouin zone was used for k-point sampling during structural optimization, and all atoms were allowed to relax. These DFT calculations were provided by the Hangzhou Yanqu Information Technology Co., Ltd (China).

2.14. Electrochemistry measurement

The electrochemical tests were all completed by an electrochemical analysis instrument (CHI660E, Shanghai, China) in the electrolyte (c($NaSO_4$) = 0.5 M). The samples of CuS, CuFC/CuS, CuFC, S–Cu–FC/CuS, and S–Cu–FC/CuS/GO were set up as working electrodes; the reference electrode was a saturated calomel electrode and a platinum plate was the auxiliary electrode. The photocurrent measurement of samples was completed under 808 nm NIR light irradiation (0.6 W cm^{-2}) for 4 off–on cycles (10 s illumination and 10 s dark).

2.15. Antibacterial experiments *in vitro*

Spread plate. All hydrogel samples were cut into uniform blocks ($3 \times 3 \times 3$ mm^3) before use. *S. aureus* (ATCC 29213) and *E. coli* (ATCC 25922) were used to evaluate the antibacterial performances of the HH hydrogel through a spread-plate method. Generally speaking, the original bacterial liquid (1.0×10^9 CFU mL^{-1}) was diluted to 1.0×10^7 CFU mL^{-1} and 200 μL of diluted liquids were taken out to submerge the samples. The samples were divided into 6 groups: Dark-control (Ctrl), Dark-GO@CMC hydrogel, Dark-HH hydrogel, Light-Ctrl, Light-GO@CMC hydrogel, and Light-HH hydrogel. After treatment with 10 min darkness or 808 nm NIR light, 20 μL was taken out from each group and diluted to 1.0×10^5 CFU mL^{-1} (NIR 808 nm: 0.6 W cm^{-2}, 10 min). Finally, 10 μL of each group was spread on an agar plate and cultured in an incubator for 24 h. Then, the antibacterial efficiency could be obtained by counting the number of colonies (N) according to the following equation: Antibacterial efficiency (%) = $(N_{Ctrl} - N_{Experiment})/N_{Ctrl} \times 100\%$.

Bacterial micromorphologies. FESEM was used to observe the changes in bacterial micromorphologies in different groups consistent with the above treatment (NIR 808 nm: 0.6 W cm^{-2}, 10 min). Bacteria in each group were fixed by glutaraldehyde (2.5%, 2 h) after antibacterial treatment. Then these bacteria were dehydrated by gradient-concentration ethanol solution (30, 50, 70, 90, and 100%) for 15 min each time. Finally, these samples were photographed by FESEM after lyophilization.

Membrane permeability test. The original *S. aureus* or *E. coli* were cultured with *o*-nitrophenyl-β-D-galactopyranoside (ONPG, 10 μg mL^{-1}) in LB medium at 37 °C for 12 h. These cultured bacteria were subjected to refrigerated centrifugation to collect the precipitation and washed twice with PBS. Then, the bacteria were dispersed with PBS and the liquid was adjusted to $OD_{600\ nm}$ = 0.05–0.1. This dispersion was used for the same antibacterial treatment as described above (NIR 808 nm: 0.6 W cm^{-2}, 10 min). Next, 15 μL of liquid of the treated bacteria was taken out from each group and mixed with 15 μL of ONPG (12.5 mM), 110 μL PBS, and 10 μL dimethyl sulfoxide (7%) to record the $OD_{420\ nm}$. Refrigerated centrifugation was carried at a speed of 6000 rpm for 5 min at 4 °C.

Protein outflow assessment. The original *S. aureus* or *E. coli* liquid was subjected to refrigerated centrifugation and washed with PBS three times. Then, the bacteria were dispersed with PBS and the liquid was adjusted to $OD_{600\ nm}$ = 0.05–0.1. This dispersion was used for the same antibacterial treatment as described above (NIR 808 nm: 0.6 W cm^{-2}, 10 min). Next, the treated bacteria in each group were subjected to refrigerated centrifugation to collect the supernatants. Then, 25 μL of supernatant was mixed with 200 μL of bicinchoninic acid (BCA) working buffer from an assay kit (cat#PC0020, Beyotime, China). These mixtures were oscillated for 30 s and incubated at 37 °C for 30 min to record the $OD_{562\ nm}$. Refrigerated centrifugation was carried at a speed of 6000 rpm for 5 min at 4 °C.

2.16. Cell experiments *in vitro*

***In vitro* biocompatibility test.** The *in vitro* biocompatibility test was carried out by the 3-[4,5-dimethylthiazol-2-yl]-2,5-diphenyltetrazolium bromide (MTT, Beyotime, China) method. GO@CMC hydrogel and HH hydrogel were co-cultured with NIH-3T3 cells for 1 day and 3 days. The medium was replaced by 200 μL of MTT solution (0.5 mg mL^{-1}) on day 1 and day 3 for 4 h incubation at 37 °C to record $OD_{490\ nm}$ or $OD_{570\ nm}$. The cell viability could be calculated according to the following equation: Cell viability (%) = $OD_{samples}/OD_{ctrl} \times 100\%$. After being irradiated on the first day for 10 min, a study of the biocompatibilities of these samples treated with NIR light (0.6 W cm^{-2}, 10 min) was performed by the same MTT method on day 1 and day 3.

Fluorescence staining *in vitro*. The hydrogels were co-cultured with NIH-3T3 cells in the same way as above for 1 day before staining. Next, the hydrogels and medium were removed before the addition of CH_2O (200 μL, 4%, PBS as solvent) for fixation (37 °C, 10 min). After that, the fixed cells were twice washed with PBS and another 100 μL of fluorescein isothiocyanate (FITC, Yeasen, China) was added to each group for 30 min incubation (37 °C) in the dark. Thereafter, the cells were washed with PBS (three times, 5 min each time) and another 10 μL of 4,6-diamidino-2-phenylindole (DAPI, Yeasen, China) were added to each group for 30 s incubation (37 °C) in the dark, which needed to be washed twice with PBS. The stained NIH-3T3 cells were photographed by an inverted fluorescence microscope (IX73, Olympus, Japan) to observe the morphologies of the cells.

2.17. Animal experiments

All-male Wister rats (180–200 g) were provided by the Tianjin Yishengyuan Biotechnology Co., Ltd (Tianjin, China). All

in vivo experiments were authorized by the Tianjin Yishengyuan Biotechnology Co., Ltd (Tianjin, China) and these animals were disposed of strictly in accordance with the relevant regulations proposed by the Ministry of Health of the People's Republic of China. The rats were fed singly in cages for 3 days to acclimate and randomly divided into three groups (n = 3): control group (Ctrl, infected mice with no treatment), 3M dressing group (infected mice treated with commercial 3M dressing), and HH hydrogel group (infected mice treated with HH hydrogel and NIR light) (NIR 808 nm: 0.6 W cm^{-2}, 10 min). After anesthesia, the rats were shaved and skin was removed by a hole punch to make wounds (diameter = 15 mm). Bacteria were then added to the wounds. Next, 10 μL of diluted bacterial solution (1×10^7 CFU mL^{-1}) was added to the wound. Then the mice were treated differently according to the groups. During the whole experiment, the operations were carried out as follows: (1) wounds were photographed on days 0, 2, 5, and 10 to record the areas; (2) the wound tissues of the mice were treated with Giemsa stain on day 2; (3) the wound tissues of the mice were treated with Masson and hematoxylin/eosin (H&E) stains on day 10; (4) the primary organs (heart, liver, spleen, lung, and kidney) of the rats were harvested on day 10 and stained with H&E; (5) whole-blood routine tests were performed on all mice on day 10. Finally, all the animals were sacrificed as required by the rules.

2.18. Statistical analysis

All the experiments were evaluated as mean values ± standard deviation of at least three tests. A one-way analysis of variance (ANOVA) program combined with a Student's t-test was used to evaluate the statistical significance of the variance ($^*P < 0.05$, $^{**}P < 0.01$, $^{***}P < 0.001$ and ns (not significant)).

3. Results and discussion

3.1. Preparation of S–Cu–FC/CuS/GO heterojunction

Firstly, the precursor CuFC was obtained through a simple hydrothermal reaction at 80 °C for 6 h with $K_4Fe(CN)_6{\cdot}3H_2O$ and $CuSO_4{\cdot}5H_2O$ as raw materials. The morphologies of CuFC powder were observed by field emission scanning electron microscopy (FESEM) and high-resolution transmission electron microscopy (HRTEM). It could be observed that the CuFC particles with a size of ~40 nm were irregularly piled up and the corresponding TEM images revealed that those CuFC particles were similar to PB, and it could be difficult to directly observe distinct lattice striations (Fig. S1†). Interestingly, it was known that both Fe^{2+} and Cu^{2+} coexist in CuFC. Considering the gradually weakened oxidation ability of Fe^{3+}, Cu^{2+} and Fe^{2+}, it could be speculated that if heating could promote the metal ions in CuFC to participate in a reaction with sulfur anions, Cu^{2+} would take precedence over Fe^{2+} to form metal sulfides (CuS or Cu_2S). Even if Fe^{2+} might be converted into Fe^{3+} ($Fe^{2+} - e^- = Fe^{3+}$), Fe^{3+} would still be reduced into divalent ions and be inferior to Cu^{2+} by the following reactions (Fig. S2†):

$$2Fe^{3+} + H_2S = 2Fe^{2+} + S + 2H^+$$

$$8Fe^{3+} + 2Cu_2S = 8Fe^{2+} + 4Cu^{2+} + 2S$$

Therefore, in these processes it could finally be considered that the sulfur anion would first complex with Cu^{2+}. Cleverly, TAA could be hydrolyzed in a heated acidic aqueous solution by the following reactions (Fig. S3†):

$$CH_3CSNH_2 + 2H_2O = NH_4{}^+ + CH_3COO^- + H_2S\uparrow$$

$$H_2S = HS^- + H^+$$

This could produce reduced sulfuric hydrogen compounds, which could precipitate metal ions.[37–39] This implied that a similar reaction between CuFC and TAA could potentially be achieved under acidic heating conditions through the following route:

$$CuFC + TAA + 2H^+ \rightarrow CuS + Fe^{2+} + H_2S\uparrow$$

Therefore, CuFC was used as a copper source to react with the S element donor, TAA, in acidic solvent (pH = 5) at 60 °C for 30 min (Fig. 1). It was expected that some of the Cu^{2+} on the surfaces of CuFC, which were complexed with $[Fe(CN)_6]^{4-}$, would react with the reducing HS^- or H_2S generated by the hydrolysis of TAA under acidic and heated conditions to form CuS and thus construct a homologous heterojunction *in situ* shared with the same copper atoms at the interface (Fig. 1a) by the following reaction:

$$Cu_2[Fe(CN)_6] + TAA \rightarrow Cu_{(2-x)}[Fe(CN)_6] - xCuS$$

Then, the morphologies of the powder produced were also observed and it was found that the products were cylindrical (length: ~180 nm, base diameter: ~50 nm) (Fig. S4a†). Meanwhile, the results of dynamic light scattering (DLS) showed that the particle size of the products was mainly 164–190 nm, much larger than that of CuFC (43.8 nm) (Fig. S4b†). It could be speculated that new chemical substances were formed on the surface of CuFC. The corresponding TEM images of the newly formed products showed distinct differences from the irregularly amorphous CuFC particles (Fig. 1b). There was also a clear boundary between two contrasting regions, representing two different substances, and lattice fringes with d-spacing of 2.78 Å could be found in the HRTEM image (Fig. 1b), which was consistent with the plane of CuS (103).[40,41] These results indicated that CuS was formed on the surface of amorphous CuFC with TAA, resulting in the *in situ* formation of a homo-heterojunction.

To clarify the real state of CuS in the product, typical CuS was further directly mixed with CuFC at room temperature to obtain a mixture labelled CuFC/CuS. The corresponding TEM and X-ray diffraction (XRD) tests were carried out (Fig. 1c and S5†). Unsurprisingly, the morphology of CuFC/CuS was similar to that of CuFC, which were disordered stacks of irregular par-

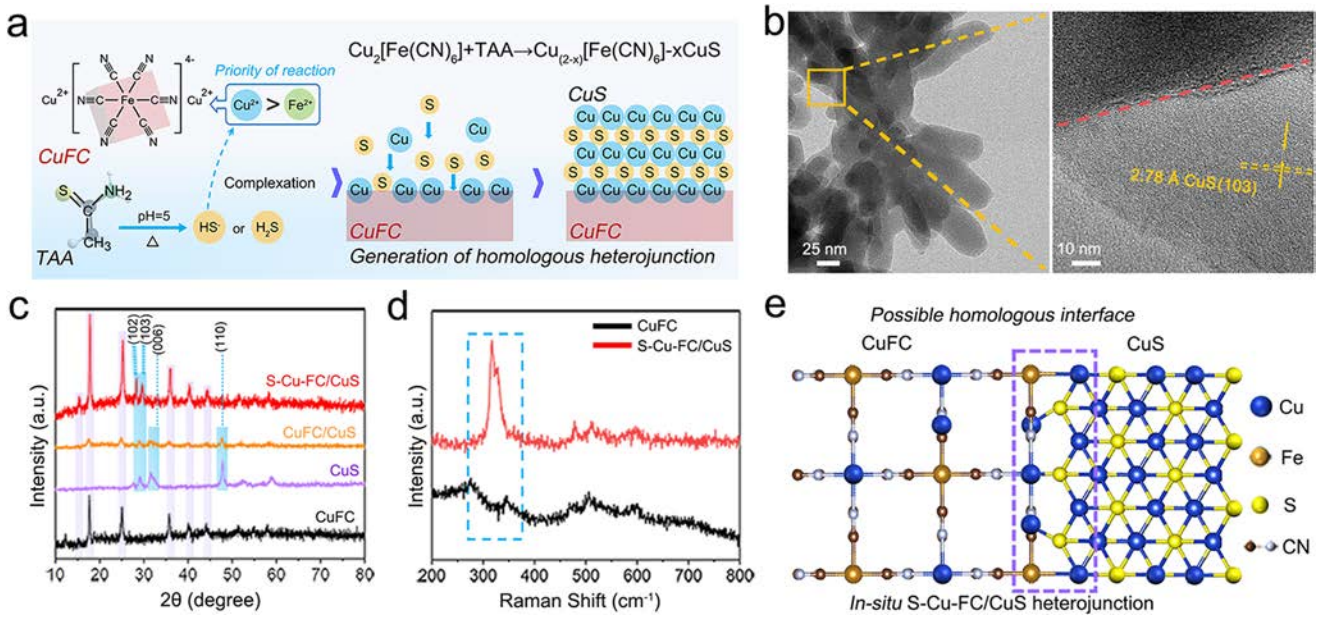

Fig. 1 Synthesis and characterization of the S–Cu–FC/CuS NPs. (a) Schematic diagram of synthesizing the heterojunction between CuFC and CuS. (b). HRTEM images of S–Cu–FC/CuS. Left scale bar is 25 nm. Right scale bar is 10 nm. (c) XRD of S–Cu–FC/CuS, CuS, CuFC/CuS, and CuFC NPs. (d) Raman spectra of S–Cu–FC/CuS and CuFC excited with 532 nm light. (e) Schematic diagram of the possible homo-heterojunction interface.

ticles and no lattice fringes of CuS could be found (Fig. S5†). This suggested that CuS was dispersed in CuFC during the direct mixing and did not change the morphology of the latter or generate a specific heterojunction. Compared with the pattern of typical CuFC, there were three new diffraction peaks belonging to the crystal planes of CuS (102), CuS (103), and CuS (100), respectively, at 28.3°, 29.7°, and 47.5° in the pattern of the *in situ* formed heterojunction (Fig. 1c). Compared with the patterns of CuS or CuFC/CuS, it was found that there were no diffraction peaks of CuS (110) and CuS (006) in the *in situ* heterojunction, indicating that the growth of CuS on the surfaces of CuFC was in a certain crystallographic orientation.[40] In addition, it was found from Fig. 1d that there was a strong characteristic peak of CuS at 350 cm^{-1} in the signals of the synthesized product compared with the Raman spectrum of the original CuFC.[41] These results confirmed that a homo-heterojunction was formed (Fig. 1e). This could be ascribed to the subsequent ionic complexation reactions. Although the Fe^{2+} in CuFC might be oxidized to Fe^{3+} by air or heating (60 °C), the H_2S produced by the hydrolysis of TAA would reduce these formed Fe^{3+} into Fe^{2+}.

Hence, it could be speculated that the Fe^{2+} did not participate in the reaction. In contrast, copper ions in CuFC exhibited stronger oxidizing ability than others, participating in a reaction with the sulfur-containing anions. Also, it could be disclosed that the reaction equilibrium would shift in favour of the generation of S–Cu–FC/CuS when H_2S was produced by the hydrolysis of TAA. This was the reason why we always could smell an odour when TAA was used in metal precipitation reactions.[38–41] Hence, it could be concluded that the *in situ* heterojunction with homologous copper atomic interfaces was successfully constructed and labelled as S–Cu–FC/CuS through a feasible addition of TAA, indicating that other ferrocyanides could potentially be used to prepare heterojunctions through similar methods, such as nickel ferrocyanide.[42,43]

3.2. Preparation of S–Cu–FC/CuS/GO@CMC hybrid hydrogel

Subsequently, the homo-heterojunction S–Cu–FC/CuS NPs were loaded onto the GO@CMC hydrogel to construct the S–Cu–FC/CuS/GO@CMC hybrid hydrogel (HH hydrogel), and tests of NIR photocatalysis were performed (Fig. 2). As shown in Fig. S6a,† a schematic diagram and SEM images demonstrated the morphologies of GO@CMC hydrogel and HH hydrogel. After the GO@CMC hydrogel was loaded with S–Cu–FC/CuS NPs, the typical folded surface of the hydrogel was covered by a large number of powder particles.[44] Meanwhile, X-ray photoelectron spectroscopy (XPS) was used to detect the elements on the surfaces of the hydrogels, and it could be seen that the new signals of S 2p, N 1s, Fe 2p, and Cu 2p, which all belonged to S–Cu–FC/CuS, appeared at 164.0 eV, 398.4 eV, 719.9 eV, and 952.2 eV, respectively (Fig. S6b†).[40,41] Similarly, the same characteristic peaks could be found both in the results of the XRD pattern of the HH hydrogel and GO@CMC hydrogel (Fig. S6c†). As shown in Fig. 2a–c, the elastic modulus of the HH hydrogel, calculated based on the slope of the stress–strain curves, was the lowest. This was because those loaded S–Cu–FC/CuS NPs enhanced the inherent strength and the relatively favorable elasticity of the GO@CMC hydrogel was retained. For the same reason, the HH hydrogel was more difficult to compress and had a relatively higher modulus of compression (Fig. 2b). The swelling capacity is another important parameter for the stability of a

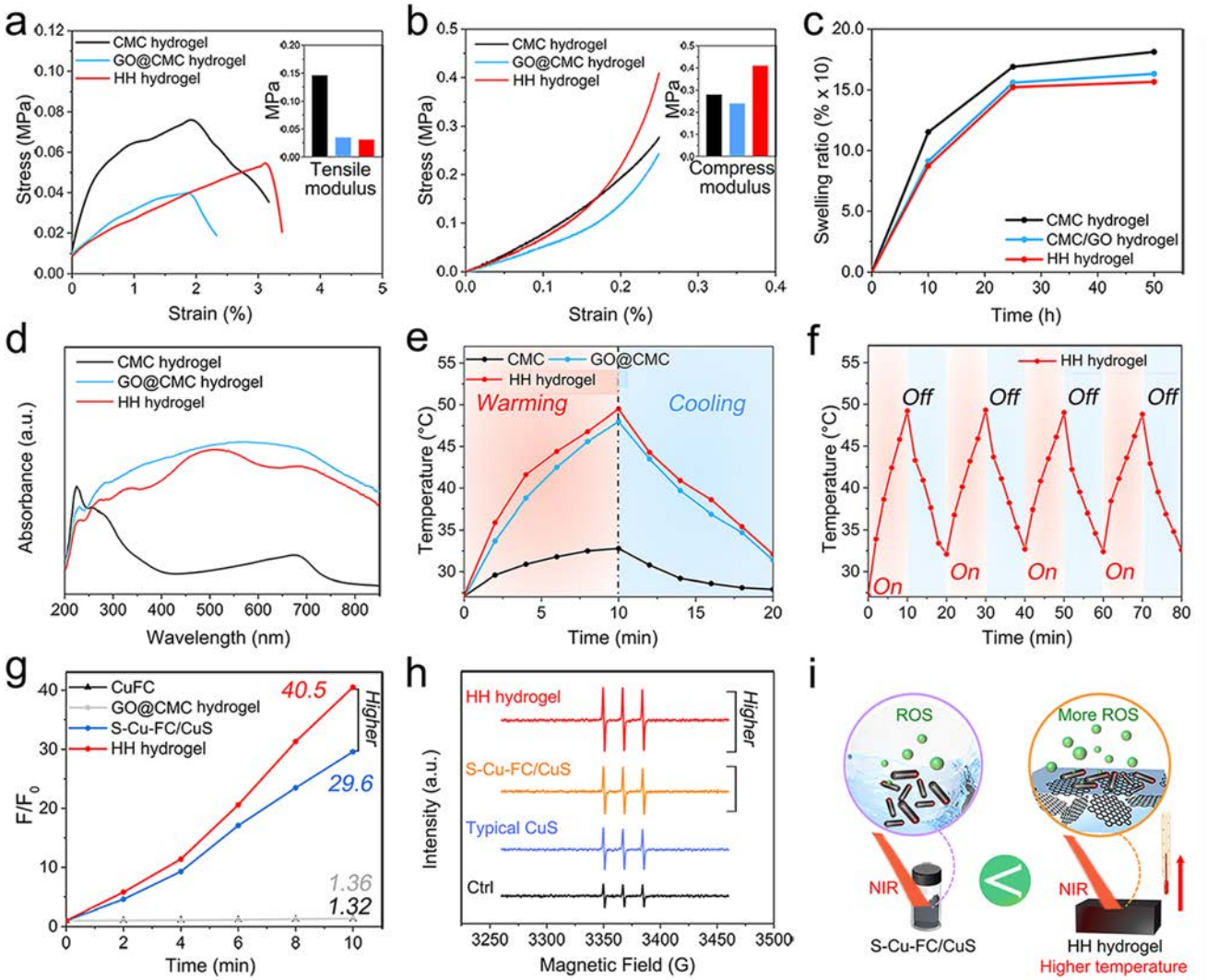

Fig. 2 Characterization and performance tests of HH hydrogel. (a) Tensile curves and tensile modulus of CMC hydrogel, GO@CMC hydrogel, and HH hydrogel. (b) Compression curves and compression modulus of CMC hydrogel, GO@CMC hydrogel, and HH hydrogel. (c) Swelling ratios of different hydrogels. (d) UV–vis spectra of different hydrogels. (e) Heating–cooling curves of different hydrogels. (f) Temperature rising and cooling profiles of HH hydrogel when the 808 nm irradiation is on/off. (g) ROS yield of CuFC, GO@CMC hydrogel, S–Cu–FC/CuS, and HH hydrogel determined by DCFH–DA. (h) ESR spectra (1 : 1 : 1, $^1O_2$) of the typical CuS, S–Cu–FC/CuS and HH hydrogel treated by TEMP. (i) Schematic diagram of the photodynamic performance differences between S–Cu–FC/CuS powder and HH hydrogel.

hydrogel. A slight reduction in overall swelling capacity occurred with the HH hydrogel, which might be induced by adsorption of a small amount of S–Cu–FC/CuS NPs into the inside of the hydrogel (Fig. 2c). But the HH hydrogel could still reach a maximum swelling rate of 1521% after 25 h in water because of its excellent and similar water absorption capacity to CMC hydrogel. These results suggested that an HH hydrogel could be constructed easily.

According to the UV test, because of being covered by S–Cu–FC/CuS NPs, the UV-vis absorption of the HH hydrogel was slightly weaker than that of the GO@CMC hydrogel; but compared with the CMC hydrogel, the HH hydrogel still showed a wide range of absorption from 200 nm to 850 nm due to the addition of GO, implying that the HH hydrogel would respond to 808 nm NIR light (Fig. 2d).[45] As shown in Fig. 2e, under 808 nm NIR illumination, the temperature of the HH hydrogel could rise to 49.5 °C, which was slightly higher than that of the GO@CMC hydrogel (48.0 °C). It might be that the S–Cu–FC/CuS NPs in the HH hydrogel also contribute an additional part of the photothermal effect.[46] In addition, the cyclic heating curve also showed that the HH hydrogel could stably heat up to about 49 °C in Fig. 2f, indicating that the HH hydrogel shows photothermal stability. Meanwhile, the photodynamic effect was investigated by a dichlorofluorescein diacetate (DCFH-DA) probe and electron spin resonance spectroscopy (ESR) with (2,2,6,6-tetramethylpiperidine (TEMP)). Firstly, after the GO@CMC hydrogel (27 mm^3, cube) was soaked with S–Cu–FC/CuS dispersion (1 mg mL^{-1}, 2 mL), the

masses of residual powders in the liquid were weighed repeatably. The loading rate of S–Cu–FC/CuS NPs in the HH hydrogel could be calculated to be about 50%. Subsequently, the HH hydrogel (27 mm^3, cube), GO@CMC hydrogel (27 mm^3, cube), S–Cu–FC/CuS NPs (1 mg, 1 mg mL^{-1}), and CuFC NPs (1 mg, 1 mg mL^{-1}) were exposed to 808 nm NIR light irradiation (0.6 W cm^{-2}) for 10 min to record the fluorescence intensities of their solutions. Interestingly, compared with the initial values, the curves of the GO@CMC hydrogel (1.36 times) and CuFC NPs (1.32 times) overlapped, indicating that they produced almost no ROS. In contrast, the S–Cu–FC/CuS NPs produced 29.6 times as much ROS while the HH hydrogel could reach 40.5 times within 10 min (Fig. 2g). Additionally, it could be seen that there were some signals of the typical $^1O_2$ (1 : 1 : 1) curves in the ESR spectra (Fig. 2h).[47] The signal intensity of the S–Cu–FC/CuS group increased by nearly two orders of magnitude compared to the control group and was even stronger than that of CuS at the same concentration (1 mg mL^{-1}), suggesting that the *in situ* formed S–Cu–FC/CuS heterojunction showed a superior photodynamic effect.[41] In addition, compared with the S–Cu–FC/CuS heterojunction, the HH hydrogel showed a stronger signal intensity consistent with the DCFH–DA test, meaning that the GO@CMC hydrogel itself did not produce ROS but could enhance the photodynamic effect of S–Cu–FC/CuS (Fig. 2i). This might be induced for the following reasons: on the one hand, the photocatalytic performance of the heterojunction was enhanced by the photothermal effect of the GO@CMC hydrogel due to its good light absorption.[27,28] On the other hand, the close contact between the GO@CMC hydrogel and S–Cu–FC/CuS could make GO act as a conductor to promote the separation of e^-/h^+ to enhance the photocatalytic reaction.

3.3. Mechanism and enhancement of photocatalysis of the homo-heterojunction

To explore the mechanisms of the photodynamic effect of the S–Cu–FC/CuS homo-heterojunction and the enhancement of the photodynamic effect, a series of further studies, including theoretical calculations, were carried out (Fig. 3). From all calculations performed in the Vienna *Ab initio* Simulation Package (VASP), the lowest-energy heterojunction interface could be constructed between the plane of CuFC (110) with 16 iron atoms, 32 copper atoms, 96 carbon atoms and 96 nitrogen atoms and the plane of CuS (001) with 60 copper atoms and 60 sulfur atoms based on density functional theory (DFT).

Moreover, the diagram of the differential charge densities revealed the gain and loss of orbital electrons at the interface between CuFC (110) and CuS (001) from different perspectives (Fig. 3a). It could be clearly observed that electron losses (irregular cyan shapes) were concentrated on the copper atoms and were mainly on the (110) side of CuFC, while the electron accumulations (irregular yellow shapes) were biased towards the CuS (001) direction. This indicated that electrons at the interface were transferred from donor CuFC to recipient CuS under NIR light. Simultaneously, in the results of the density of states (DOS), it could be seen that the order of the number of electrons provided by the hybrid orbitals was Cu-3d, Fe-3d, N-2p, S-2p, and C-2s, when the horizontal coordinate of 0 eV was taken as the reference point (Fig. 3a).[33,41,45,48] This implied that more electron donors were concentrated on the orbitals of copper atoms and iron atoms, which was consistent with the differential charge densities. Therefore, due to the growth of the *in situ* S–Cu–FC/CuS heterojunction, the interfacial copper atoms played the roles of electron donor and electron acceptor as the homologous substance of the CuFC and CuS, inducing more electrons to enter CuS to participate in the photocatalytic process. Meanwhile, a photocurrent test of S–Cu–FC/CuS and CuFC/CuS was conducted. As shown in Fig. 3b, the photocurrent intensity in S–Cu–FC/CuS was the highest among the measured values from CuFC, CuS, and CuFC/CuS. There were some photocurrents under NIR illumination in CuS while the photocurrent disappeared after CuS was mixed with CuFC. These results implied that the spatial charge separation ability of this formed homogeneous heterojunction was faster than that of CuS alone because of the important homogeneous-interfacial copper atoms, which was consistent with the DFT calculation. It also demonstrated that the photodynamic effect of S–Cu–FC/CuS was superior to that of CuS due to the method of constructing the homologous heterojunction by ion complexation. Then, the enhancement of the photodynamic effect was further explored. Based on the known loading rate of S–Cu–FC/CuS NPs being 50% and the measured volume of the GO@CMC hydrogel after drying being 1/20 of the volume of the original mixture, it could be calculated that there was approximately 0.265 mg of GO which was in contact with S–Cu–FC/CuS NPs after immersion in GO@CMC hydrogel. To explore the changes in the photodynamic effect induced by the close contact between S–Cu–FC/CuS and GO, ternary S–Cu–FC/CuS/GO NPs were constructed at room temperature. The UV–vis curve of S–Cu–FC/CuS NPs not only retained the original absorption region of CuFC (400–600 nm), but the heterojunction also showed a new absorption region around 800 nm, indicating the d–d transition of Cu^{2+} induced by the *in situ* CuS (Fig. 3c).[40]

Also, after the heterojunction was combined with GO, S–Cu–FC/CuS/GO still showed good absorption around 800 nm. The energy gaps (E_g) of CuFC, S–Cu–FC/CuS, and S–Cu–FC/CuS/GO could be calculated to be 2.28 eV, 1.48 eV, and 1.44 eV, respectively (Fig. S7†). The different E_g of these samples proved that, after being combined with GO, the gap of S–Cu–FC/CuS became narrower, allowing electrons to cross the band gap more easily to participate in photocatalytic reactions. In subsequent electrochemical tests, ternary S–Cu–FC/CuS/GO not only showed the strongest photocurrent density but also the smallest electrochemical impedance compared with S–Cu–FC/CuS and CuFC. This result revealed that GO could enhance the spatial charge separation ability and reduce the charge transfer resistance of S–Cu–FC/CuS and consequently allow electrons to move faster (Fig. 3d and e). Photothermal tests proved that the addition of GO enhanced the photothermal effect of S–Cu–FC/CuS (Fig. S8†). It had been reported that electron motion in CuS could also be enhanced by the photothermic effect of

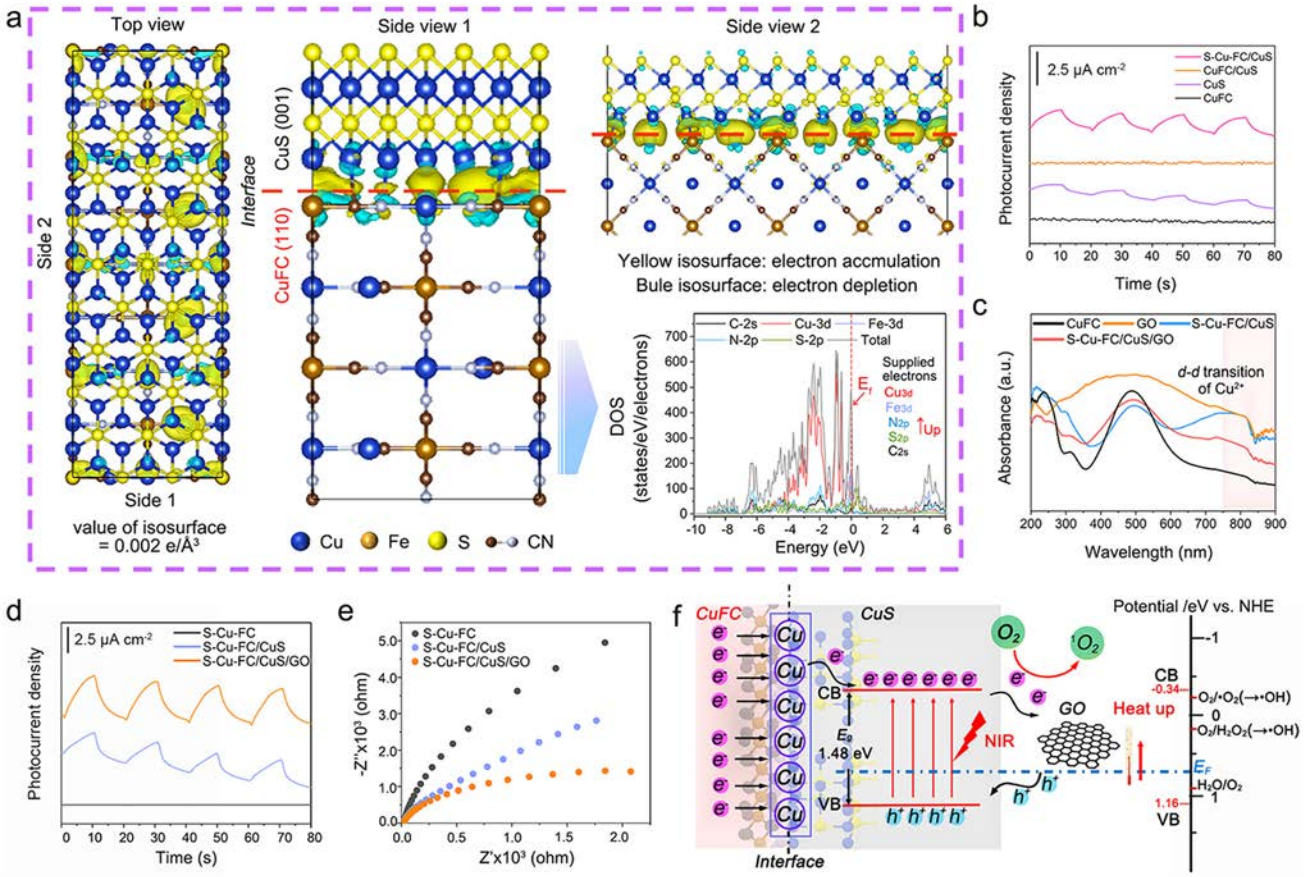

Fig. 3 Photocatalysis mechanisms of S–Cu–FC/CuS NPs and HH hydrogel. (a) DFT calculation of the S–Cu–FC/CuS structure and corresponding differential charge density and DOS. (b) Photocurrent response of CuFC, CuS, CuFC/CuS, and S–Cu–FC/CuS under 808 nm NIR irradiation. (c) UV–vis spectrum of GO, CuFC, S–Cu–FC/CuS, and S–Cu–FC/CuS/GO. (d) Photocurrent response of CuFC, S–Cu–FC/CuS, and S–Cu–FC/CuS/GO under 808 nm NIR irradiation. (e) EIS tests of CuFC, S–Cu–FC/CuS, and S–Cu–FC/CuS/GO. (f) Mechanism of the photothermic enhanced photodynamic effect of S–Cu–FC/CuS and HH hydrogel.

GO.[49] This suggested that the close contact between GO and S–Cu–FC/CuS in the HH hydrogel might not be as sufficient as ternary S–Cu–FC/CuS/GO and it was still reasonable to believe that the photodynamic effect of S–Cu–FC/CuS loaded with GO@CMC hydrogel was enhanced by GO in some aspects. Therefore, the potential mechanism of the enhanced photodynamic effect is schematically illustrated in Fig. 3f. Benefiting from the *in situ* formed S–Cu–FC/CuS, interfacial copper atoms acted as both donors and acceptors to continuously supply electrons from the non-photocatalytic CuFC to the photocatalytic CuS to produce ROS under NIR irradiation. And because of the close contact of S–Cu–FC/CuS and GO in the HH hydrogel, the electron–hole separation ability and faster carrier transfer of S–Cu–FC/CuS were enhanced by the photothermal effect of GO.[49] Eventually, the photodynamic performance of the HH hydrogel was significantly promoted relative to S–Cu–FC/CuS NPs.

3.4. *In vitro* sterilization by HH hydrogel

Two typical Gram-positive and Gram-negative bacteria, *S. aureus* and *E. coli*, were chosen to evaluate the antibacterial performance of the HH hydrogel (Fig. 4). After 10 min of NIR irradiation (0.6 W cm^{-2}), it could be observed that the HH hydrogel exhibited the highest sterilization rate (99.5%) to *S. aureus* in Fig. 4a, while single PTT achieved only 33.2% antibacterial rate in the Light-GO@CMC hydrogel group.

As shown in the corresponding FESEM images (Fig. 4b), the number of dead *S. aureus* with ruptured and atrophied membranes (yellow arrows) was much greater in the Light-HH hydrogel group than that in the other groups. Similarly, the HH hydrogel could achieve 100.0% sterilization rate against *E. coli* under NIR irradiation (Fig. 4c), and approximately 60% of the bacteria were killed by single PTT in the Light-GO@CMC hydrogel group. The number of wrinkled or twisted *E. coli* (yellow arrows) in the Light-HH hydrogel group was far greater than the numbers in the other groups (Fig. 4d). These results proved that the HH hydrogel showed an excellent rapid NIR sterilization ability. Meanwhile, there were 37.6% *S. aureus* and 48.3% *E. coli* sterilized, respectively, in the Dark-HH hydrogel groups, while the other groups in the dark showed no obvious antibacterial ability. This sterilization might be contributed by positive S–Cu–FC/CuS NPs on the

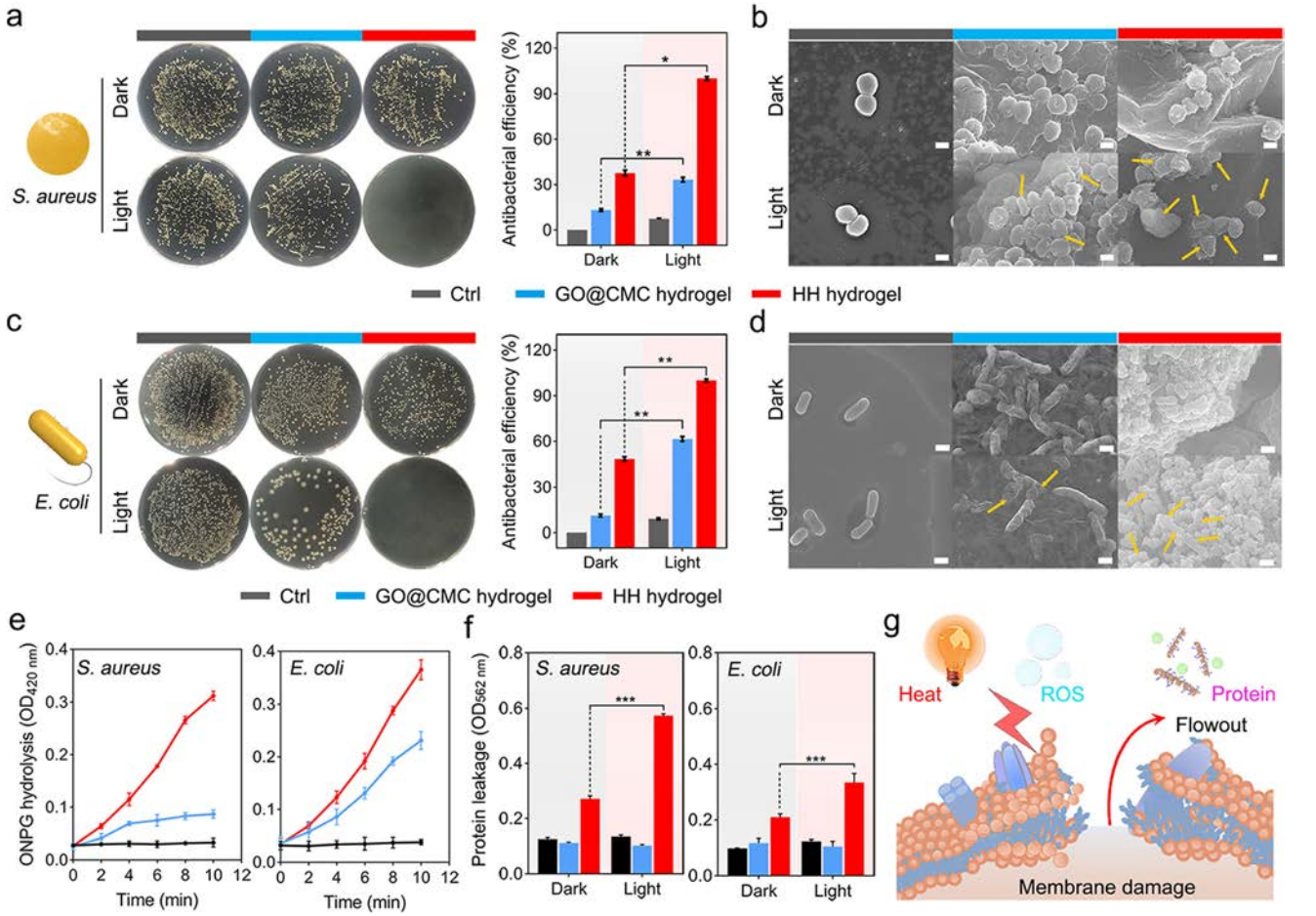

Fig. 4 *In vitro* antibacterial tests of HH hydrogel. (a) Photographs and antibacterial efficiency of spread-plate experiment for *S. aureus* in different groups. (b) Corresponding SEM images of *S. aureus* in (a). All scale bars are 1 μm. Yellow arrows represent bacteria with broken membranes. (c) Photographs and antibacterial efficiency of spread-plate experiment for *E. coli* in different groups. (d) Corresponding SEM images of *E. coli* in (c). All scale bars are 1 μm. Yellow arrows represent bacteria with broken membranes. (e) ONPG analysis of *S. aureus* and *E. coli* in different groups of samples with 808 nm NIR irradiation for 10 min. (f) BCA test of *S. aureus* and *E. coli* in different groups of samples without and with 808 nm NIR irradiation for 10 min. (g) Schematic diagram of the antibacterial mechanism. Statistical differences were analyzed by one-way ANOVA and *post hoc* Tukey's test: $*P < 0.05$, $**P < 0.01$, $***P < 0.001$, and ns (not significant).

surface of the hybrid hydrogel and a small amount of Cu^{2+} released from CuS.[50]

To investigate the antibacterial mechanism of the HH hydrogel under NIR irradiation, ONPG and BCA tests were carried out to detect the membrane permeability ($OD_{420\ nm}$) and the protein outflow ($OD_{562\ nm}$) of the bacteria, respectively. As shown in Fig. 4e, the membrane permeabilities of *S. aureus* and *E. coli* were significantly increased compared to the photothermal GO@CMC hydrogel groups or control groups after 10 min of irradiation. This revealed that the bacterial membranes could not be effectively destroyed by PTT alone, but they were promptly damaged by the ROS and heat generated by the synergetic PTT/PDT of the HH hydrogel. The results of the BCA tests were similar to the trend of ONPG and spread-plate tests (Fig. 4f); there was a slight outflow of bacterial proteins caused by the hybrid hydrogels in the dark, and their protein outflow increased sharply after treatment with NIR irradiation.

These results revealed that the bacterial membrane could not be effectively destroyed by PTT alone, but the bacterial integrity was seriously damaged by the ROS and heat generated from the synergistic PTT/PDT, causing massive outflow of internal substances to sterilize pathogens rapidly (Fig. 4g).[51]

3.5. Biocompatibility and *in vivo* sterilization by the HH hydrogel

The *in vitro* biocompatibility of the hydrogels was tested through an ICP test and the MTT method (Fig. 5 and S9†). Ions released from the HH hydrogel were examined *in vitro* within 14 days, and the final concentrations of Cu^{2+} and Fe^{2+} were 0.165 mg L^{-1} and 0.137 mg L^{-1} on day 14, respectively (Fig. S9†). This indicated that the released Cu^{2+} and Fe^{2+} might promote wound healing through accelerating the formation of blood vessels and the synthesis of hemoglobin.[52] At the same time, an MTT assay was conducted on the GO@CMC hydrogel and HH hydrogel with NIH-3T3 cells before the

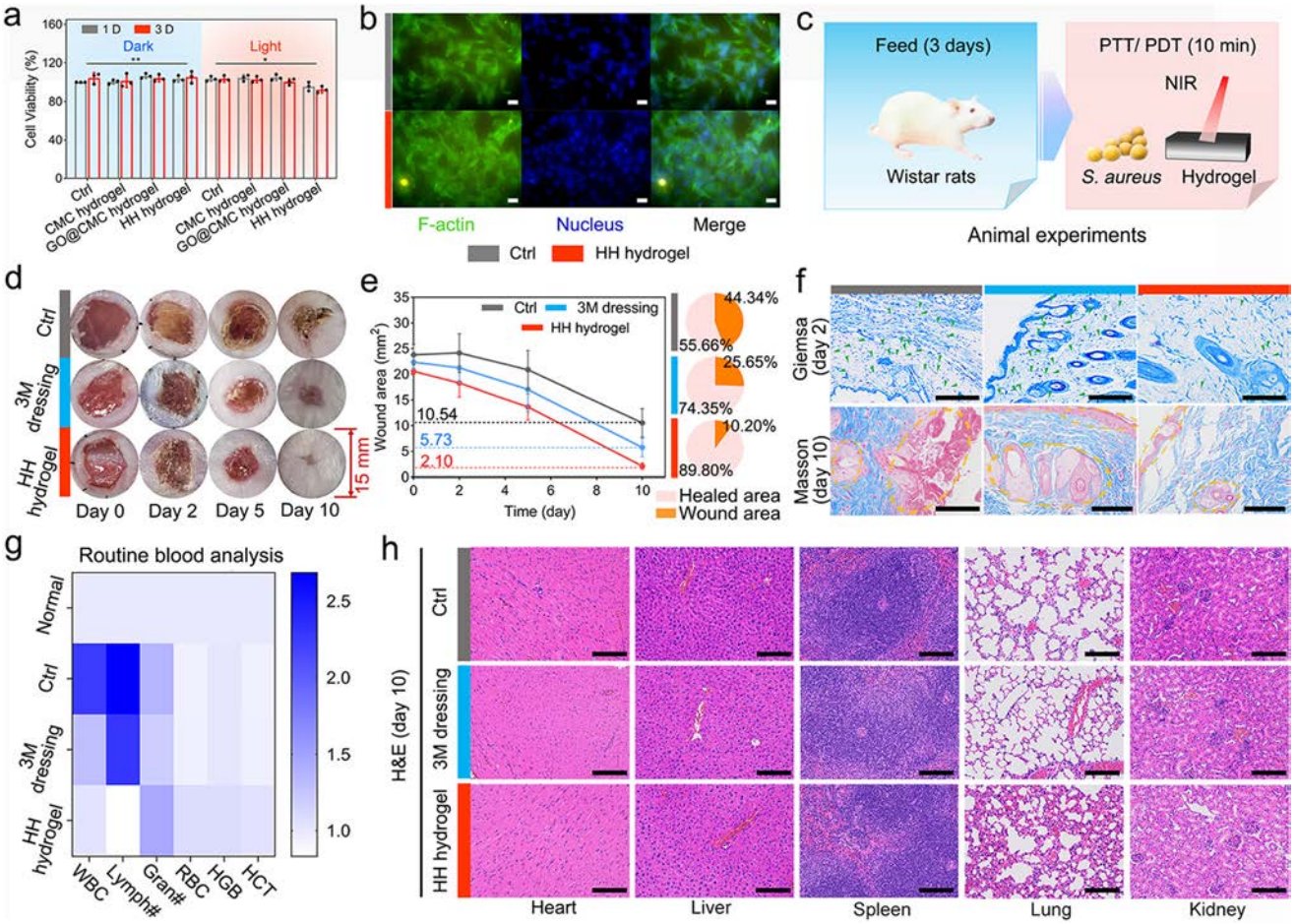

Fig. 5 *In vitro* biocompatibility assay and *in vivo* wound healing test of HH hydrogel. (a) MTT assay of NIH-3T3 cells treated by different samples and conditions. (b) Fluorescence images of NIH-3T3 cells co-cultured with or without HH hydrogel for 1 day *in vitro*. Scale bars are all 50 μm. (c) Schematic diagram of the antibacterial test of PTT/PDT induced by HH hydrogel *in vivo*. (d) Photographs of wounds in different groups at days 0 2, 5, and 10. (e) Quantitative results of wound areas and final healing rates of different groups. (f) Giemsa stain images of residual bacteria in a wound at day 2 (green arrows) and Masson stained images of different groups at day 10. Scales bars are all 200 μm. (g) Routine blood analysis of rats in different groups at day 10. (h) H&E staining of main organs in different groups at day 10. Scale bars are all 100 μm. Statistical differences were analyzed by one-way ANOVA and *post hoc* Tukey's test: $*P < 0.05$, $**P < 0.01$, $***P < 0.001$, and ns (not significant).

in vivo experiment. As shown in Fig. 5a, both the GO@CMC hydrogel and the HH hydrogel showed good biocompatibility after 24 h or 72 h of co-culture in the dark, implying that continuously released metal ions were not biotoxic. On day 1 after irradiation, the cell activity of the HH hydrogel group was slightly lower than that of other groups on day 3, possibly because the heat and ROS generated by PTT/PDT slowed cell proliferation while still maintaining good biocompatibility.[53] Additionally, FITC and DAPI staining were used to observe the morphologies of co-cultured cells for 1 day, and it could be observed that the cells in all groups were in a pseudopod-extended spreading state, proving the good biocompatibility of the HH hydrogel (Fig. 5b).[54]

Then, to evaluate the antibacterial performance of the HH hydrogel *in vivo*, bacteria-infected wounds (diameter = 15 mm) were created on the back of Wister rats. All the rats were randomly divided into three groups according to the different treatments: control group (without treatment), 3M dressing group (treated with commercial 3M dressing), and HH hydrogel group (treated with HH hydrogel and 10 min of NIR irradiation) (Fig. 5c). As shown in Fig. 5d and e, wound healings of all rats were recorded and quantified during these 10 days. It was found that the reduction of wound areas in the HH hydrogel group was fastest during the therapy process and the corresponding final healing rate of the HH hydrogel group (90%) was significantly higher than that of both 3M dressing (74%) and the Ctrl groups (55%), and there also remained heavily crusted and unhealed wounds on the backs of rats in the control group (Ctrl) and 3M dressing group on day 10. These results indicated that the synergistic PTT/PDT induced by HH hydrogel could effectively promote the healing of bacteria-infected wounds. Moreover, the wound tissues of rats at different time stages were stained to further evaluate the infection, inflammation and recovery of the wounds. As shown in

the day-2 Giemsa-stained images, a large amount of small ball-like *S. aureus* (green arrows) was alive in the wound tissues of the control and 3M dressing groups, while in contrast only a few residual pathogens could be found in the HH hydrogel group after treatment on the first day (Fig. 5f). This was consistent with the *in vitro* spread-plate test, suggesting that this rapid phototherapy could remove bacteria *in vivo*. The day-10 inflammation of wound tissues was investigated through H&E staining, and the number of semilunar neutrophils in the HH hydrogel group was the lowest, indicating that the inflammation was significantly relieved because of the rapid disinfection by the HH hydrogel (Fig. S10†).[7] Then, Masson stain was used in the evaluation of day-10 wound repair (Fig. 5f). In the Ctrl and 3M dressing groups, the muscle fibres were stained red, while collagen fibres that occupied a small area were stained blue. In contrast, blue collagen fibres occupied the greatest area in the HH hydrogel group, indicating an abundance of collagen fibres deposited in the tissue and that the wounds healed satisfactorily.[7]

Additionally, the blood and major organs of rats were tested on day 10 to evaluate the *in vivo* biocompatibility. As far as we know, if bacterial infection occurred, the immune system would defend against causative agents by producing numerous white blood cells (WBCs), including neutrophils and lymphocytes. As shown in Fig. 5g, the numbers of WBCs, neutrophils and lymphocytes in Ctrl and 3M dressing groups were significantly higher than that of the HH hydrogel group, meaning that those rats in the first two groups still retained severe bacterial infections, which was consistent with the previous results of Giemsa and H&E staining. And the values of hemoglobin (HGB) concentration, red blood cells (RBC), and hematocrit (HCT) in the HH hydrogel group recovered to a similar level to normal rats but were slightly higher than those of the Ctrl and 3M groups, indicating that the metal ions released from the HH hydrogel could effectively promote wound healing.[55] Meanwhile, the day-10 H&E staining of the rats' main organs showed that there was no noticeable damage caused in the HH hydrogel group after treatment. All the results suggested that the HH hydrogel was biosafe *in vivo* and could be used for the long-term treatment of bacterially infected wounds (Fig. 5h).

4. Conclusion

In summary, we for the first time prepared an *in situ* homo-heterojunction based on the priority of metal ions involved in complexation reactions by using CuFC as a copper source to endow this ferrocyanide with NIR photocatalytic activity. This homo-heterojunction was successfully combined with GO@CMC hydrogel to construct an HH hydrogel, which enhanced the photocatalytic activity of the homologous S–Cu–FC/CuS interface through GO-induced faster transfer and its photothermal effect. The hydrogel-guided synergistic PTT/PDT was successfully used *in vitro* and *in vivo* for rapid sterilization therapy and promotion of the healing of bacteria-infected wounds. Although this design of heterojunctions for NIR photocatalytic response has only been successfully achieved on CuFC at present, it will provide a novel direction for imparting photocatalytic performance to a range of other ferrocyanides. This study also provides more options for designing a better photothermal-photodynamic hydrogel for biomedical applications.

Author contributions

B.H., W.G., S.W., and X.L. designed and developed the concepts of all experiments. B.H. and W.G. performed the preparations and characterizations of samples. B.H., W.G., S.W., and X.L. analysed the data and cowrote the manuscript. C.W., Z.C., Y.Z., Z.L., S.Z., J.H., and P.K.C. provided important insights. The manuscript was discussed by all the authors.

Ethical statement

The rats were purchased form Tianjin Yishengyuan Biotechnology Co., Ltd (Tianjin, China). All animal procedures were performed in accordance with Animal Management Rules of the Ministry of Health of the People's Republic of China and approved by the Animal Ethics Committee of Tianjin Yishengyuan Biotechnology Co., Ltd (Animal experiment license key: SYXK 2021-0003).

Conflicts of interest

There are no conflicts to declare.

Acknowledgements

This work is jointly supported by the National Natural Science Foundation of China (No. 52173251, 51871162, and 82002303), the China National Funds for Distinguished Young Scientists (No. 51925104), NSFC-Guangdong Province Joint Program (Key program no. U21A2084), the Central Guidance on Local Science and Technology Development Fund of Hebei Province (226Z1303G), and Guangdong Basic and Applied Basic Research Foundation (2021A1515220093, 2022A1515011536).

References

1 T. C. Pierson and M. S. Diamond, *Nat. Microbiol.*, 2020, **5**, 796–812.
2 H. M. Zowawi, P. N. A. Harris, M. J. Roberts, P. A. Tambyah, M. A. Schembri, M. D. Pezzari, D. A. Williamson and D. L. Paterson, *Nat. Rev. Urol.*, 2015, **12**, 570–584.
3 D. M. Morens, G. K. Folkers and A. S. Fauci, *Nature*, 2004, **430**, 242–249.

4 A. Josephson, T. Kilic and J. D. Michler, *Nat. Hum. Behav.*, 2021, **5**, 557–565.
5 World Health Organization, COVID-19 pandemic: **https://www.who.int/emergencies/diseases/novelcoronavirus-2019**.
6 F. Zhou, T. Yu, R. Du, G. Fan, Y. Liu, Z. Liu, J. Xiang, Y. Wang, B. Song, X. Gu, L. Guan, Y. Wei, H. Li, X. Wu, S. Tu, Y. Zhang, H. Chen and B. Cao, *Lancet*, 2020, **395**, 1054–1062.
7 J. Li, Z. Li, X. Liu, C. Li, Y. Zheng, K. W. K. Yeung, Z. Cui, Y. Liang, S. Zhu, W. Hu, Y. Qi, T. Zhang, X. Wang and S. Wu, *Nat. Commun.*, 2021, **12**, 1224.
8 C. Hobson, A. N. Chan and G. D. Wright, *Chem. Rev.*, 2021, **121**, 3464–3494.
9 I. Chopra, C. Schofield, M. Everett, A. O'Neill, K. Miller, M. Wilcox, J. Frère, M. Dawson, L. Czaplewski, U. Urleb and P. Courvalin, *Lancet Infect. Dis.*, 2008, **8**, 133–139.
10 X. Li, J. F. Lovell, J. Yoon and X. Chen, *Nat. Rev. Clin. Oncol.*, 2020, **17**, 657–674.
11 M. Chang, Z. Hou, M. Wang, C. Yang, R. Wang, F. Li, T. Peng, C. Li and J. Lin, *Angew. Chem.*, 2021, **133**, 13081–13089.
12 Z. Wang, B. Liu, Q. Sun, L. Feng, F. He, P. Yang, S. Gai, Z. Quan and J. Lin, *ACS Nano*, 2021, **7**, 12342–12357.
13 J. Yan, B. Li, P. Yang, J. Lin and Y. Dai, *Adv. Funct. Mater.*, 2021, **31**, 2104325.
14 F. Zeng, L. Tang, Q. Zhang, C. Shi, Z. Huang, S. Nijiati, X. Chen and Z. Zhou, *Angew. Chem.*, 2022, **134**, e202112925.
15 H. P. Lee and A. K. Gaharwar, *Adv. Sci.*, 2020, **7**, 2000863.
16 C. Ding, Y. Huang, Z. Shen and X. Chen, *Adv. Mater.*, 2021, **33**, 2007768.
17 J. Huo, Q. Jia, H. Huang, J. Zhang, P. Li, X. Dong and W. Huang, *Chem. Soc. Rev.*, 2021, **50**, 8762–8789.
18 Z. Hou, Y. Wu, C. Xu, S. Reghu, Z. Shang, J. Chen, D. Pranantyo, K. Marimuth, P. P. De, O. T. Neg, K. Pethe, E. Kang, P. Li and M. B. Chen-park, *ACS Cent. Sci.*, 2020, **11**, 2031–2045.
19 J. Zhang, Q. Jia, Z. Yue, J. Huo, J. Chai, L. Yu, R. Nie, H. Shao, Y. Zhao, P. Li and W. Huang, *Adv. Mater.*, 2022, **34**, 2200334.
20 K. Tao, Z. Chen, J. Yu, H. Zeng, J. Wu, Z. Wu, Q. Jia, P. Li, Y. Fu, H. Chang and W. Yuan, *Adv. Sci.*, 2022, **9**, 2104168.
21 C. Wang, Y. Luo, X. Liu, Z. Cui, Y. Zheng, Y. Liang, Z. Li, S. Zhu, J. Lei, X. Feng and S. Wu, *Bioact. Mater.*, 2022, **13**, 200–211.
22 W. Guan, L. Tan, X. Liu, Z. Cui, Y. Zheng, K. W. K. Yeung, D. Zheng, Y. Liang, Z. Li, S. Zhu, X. Wang and S. Wu, *Adv. Mater.*, 2021, **33**, 2006047.
23 Y. Li, X. Liu, B. Li, Y. Zheng, Y. Han, D. Chen, K. W. K. Yeung, Z. Cui, Y. Liang, Z. Li, S. Zhu, X. Wang and S. Wu, *ACS Nano*, 2020, **14**, 8157–8170.
24 L. An, C. Wang, Q. Tian, C. Tao, F. Xue, S. Yang, X. Zhou, X. Chen and G. Huang, *Nano Today*, 2022, **43**, 101397.
25 S. Zhang, M. Du, Z. Xing, Z. Li, K. Pana and W. Zhou, *Appl. Catal., B*, 2020, **262**, 118202.
26 Y. Jin, Z. Lu, P. Zhang, F. Li, T. Li, L. Zhang, W. Fan and C. Hu, *J. Hazard. Mater.*, 2022, **424**, 127502.
27 D. Han, Y. Han, J. Li, X. Liu, K. W. K. Yeung, Y. Zheng, Z. Cui, X. Yang, Y. Liang, Z. Li, S. Zhu, X. Yuan, X. Feng, C. Yang and S. Wu, *Appl. Catal., B*, 2020, **261**, 118248.
28 D. Han, Y. Li, X. Liu, K. W. K. Yeung, Y. Zheng, Z. Cui, Y. Liang, Z. Li, S. Zhu, X. Wang and S. Wu, *J. Mater. Sci. Technol.*, 2021, **62**, 83–95.
29 S. Ayrault, B. Jimenez, E. Garnier, M. Fedoroff, D. J. Jones and C. Loos-Neskovic, *J. Solid State Chem.*, 1998, **141**, 475–485.
30 H. H. Someda, A. A. ElZahhar, M. K. Shehata and H. A. El-Naggar, *Sep. Purif. Technol.*, 2002, **29**, 53–61.
31 T. Sangvanich, V. Sukwarotwat, R. J. Wiacek, R. M. Grudzien, G. E. Fryxell, R. S. Addleman, C. Timchalk and W. Yantassee, *J. Hazard. Mater.*, 2010, **182**, 225–231.
32 F. Han, G. H. Zhang and P. Gu, *J. Radioanal. Nucl. Chem.*, 2013, **295**, 369–377.
33 J. Li, X. Liu, L. Tan, Z. Cui, X. Yang, Y. Liang, Z. Li, S. Zhu, Y. Zheng, K. W. K. Yeung, X. Wang and S. Wu, *Nat. Commun.*, 2019, **10**, 4490.
34 W. Wu, L. Yu, Y. Pu, H. Yao, Y. Chen and J. Shi, *Adv. Mater.*, 2020, **32**, 2000542.
35 X. Cai, W. Gao, M. Ma, M. Wu, L. Zhang, Y. Zheng, H. Chen and J. Shi, *Adv. Mater.*, 2015, **27**, 6382–6389.
36 Z. Yang, W. Tian, Q. Wang, Y. Zhao, Y. Zhang, Y. Tian, Y. Tang, S. Wang, Y. Liu, Q. Ni, G. M. Lu, Z. Teng and L. Zhang, *Adv. Sci.*, 2018, **5**, 1700847.
37 E. J. Hartvng, *Trans. Faraday Soc.*, 1920, **15**, 160–177.
38 D. Lu, W. Wang, Y. Chang, F. Xie and K. Jiang, *Metals*, 2016, **6**, 303.
39 H. Zhou, H. Xiong, R. Zhang, L. Zhang, L. Zhang, L. Li, W. Zhang, Z. Zhu and Z. Qiao, *Small*, 2021, **7**, 2100428.
40 Q. Tian, M. Tang, Y. Sun, R. Zou, Z. Chen, M. Zhu, S. Yang, J. Wang and J. Hu, *Adv. Mater.*, 2011, **23**, 3542–3547.
41 H. Liu, J. Li, X. Liu, Z. Li, Y. Zhang, Y. Liang, Y. Zheng, S. Zhu, Z. Cui and S. Wu, *ACS Nano*, 2021, **15**, 18505–18519.
42 W. P. Iverson, *Nature*, 1967, **13**, 486–487.
43 S. K. Geng, Y. Zheng, S. Q. Li, H. Su and X. Zhao, *Nat. Energy*, 2021, **6**, 904–912.
44 C. Wang, M. Fadeev, M. Vazquez-Gonzalez and I. Willner, *Adv. Funct. Mater.*, 2018, **28**, 1803111.
45 Y. Li, X. Liu, L. Tan, Z. Cui, X. Yang, Y. Zheng, K. W. K. Yeung, P. K. Chu and S. Wu, *Adv. Funct. Mater.*, 2018, **28**, 1800299.
46 A. Curcio, A. V. Walle, E. Benassai, A. Serrano, N. Luciani, N. Menguy, B. B. Manshian, A. Sargsian, S. Soenen, A. Espinosa, A. Abou-Hassan and C. Wilhelm, *ACS Nano*, 2021, **15**, 9782–9795.
47 S. Wang, A. Riedinger, H. Li, C. Fu, H. Liu, L. Li, T. Liu, L. Tan, M. J. Barthel, G. Pugliese, F. D. Donato, M. S. Dá$\frac{31}{42}$Abbusco, X. Meng, L. Manna, H. Meng and T. Pellegrino, *ACS Nano*, 2015, **9**, 1788–1800.
48 R. M. Cordova-Castro, M. Casavola, M. V. Schilfgaarde, A. V. Krasavin, M. A. Green, D. Richards and A. V. Zayats, *ACS Nano*, 2019, **13**, 6550–6560.

49 Z. Gan, X. Wu, M. Meng, X. Zhu, L. Yang and P. K. Chu, *ACS Nano*, 2014, **8**, 9304–9310.
50 P. Tsvetkov, S. Coy, B. Petrova, M. Dreishpoon, A. Verma, M. Abdusamad, J. Rossen, L. Joesch-choen, R. Humeidi, R. D. Spangler, J. K. Eaton, E. Frenkel, M. Kocak, S. M. Corsello, S. Lutsenko, N. Kanarek, S. Santagata and T. R. Golub, *Science*, 2022, **375**, 1254–1261.
51 T. M. Gross, J. Lahiri, A. Golas, J. Luo, F. Verrier, J. L. Kurzejewski, D. E. Baker, J. Wang, P. F. Novak and M. J. Snyder, *Nat. Commun.*, 2019, **10**, 1979.
52 Y. Li, R. Fu, Z. Duan, C. Zhu and D. Fan, *ACS Nano*, 2022, **16**, 7486–7502.
53 Y. Qiao, X. Liu, B. Li, Y. Han, Y. Zheng, K. W. K. Yeung, C. Li, Z. Cui, Y. Liang, Z. Li, S. Zhu, X. Wang and S. Wu, *Nat. Commun.*, 2020, **11**, 4446.
54 Y. Yuan, S. Shen and D. Fan, *Biomaterials*, 2021, **276**, 120838.
55 R. Yang, G. Li, C. Zhuang, P. Yu, T. Ye, Y. Zhang, P. Shang, J. J. Huang, M. Gai, L. Wang, W. Cui and L. Deng, *Sci. Adv.*, 2021, **7**, eabg3816.